2002 HST Calibration Workshop
Space Telescope Science Institute, 2002
S. Arribas, A. Koekemoer, and B. Whitmore, eds.

Coronagraphic Imaging with *HST* and STIS[1,2]

C. A. Grady

NOAO, Eureka Scientific and GSFC, Code 681, NASA's GSFC, Greenbelt, MD 20771; cgrady@echelle.gsfc.nasa.gov

C. Proffitt

Space Telescope Science Institute, 3700 San Martin Dr., Baltimore, MD 21218

E. Malumuth

Science Systems and Applications, Inc., Lanham, MD 20706

B. E. Woodgate, T. R. Gull, C. W. Bowers, S. R. Heap, and R. A. Kimble

Code 681, Laboratory for Astronomy & Solar Physics, NASA's GSFC, Greenbelt, MD 20771; members of the Space Telescope Imaging Spectrograph Investigation Definition Team

D. Lindler

Sigma Research and Engineering, Lanham, MD 20706

P. Plait

Department of Physics and Astronomy, Sonoma State University, Rohnert Park, CA 94928

Abstract. Revealing faint circumstellar nebulosity and faint stellar or substellar companions to bright stars typically requires use of techniques for rejecting the direct, scattered, and diffracted light of the star. One such technique is Lyot coronagraphy. We summarize the performance of the white-light coronagraphic capability of the Space Telescope Imaging Spectrograph, on board the *Hubble Space Telescope*.

1. Introduction

As part of its optical imaging capabilities, the Space Telescope Imaging Spectrograph (STIS) is equipped with an opaque focal plane mask to occult the star, a sub-aperture, circular, pupil plane mask, and an unfiltered CCD providing a simple white-light coronagraph (Woodgate et al. 1998; Kimble et al. 1998). Fig. 1 shows a simplified version of the STIS optical path for coronagraphic observations (after Heap, et al. 2000). The bandpass of the coronagraph is CCD-limited to 0.2–1.0 μm with $\lambda_{\rm eff} \approx 5875$ Å. Since 1997, the STIS coronagraph has been used to image reflection nebulosity, protoplanetary disks, emission line

[1]Based on observations made with the NASA/ESA *Hubble Space Telescope*, obtained at the Space Telescope Science Institute, which is operated by the Association of Universities for Research in Astronomy, Inc., under NASA Contract NAS5-26555.

[2]Data included in this study come in part from the STIS IDT protoplanetary disk key project.

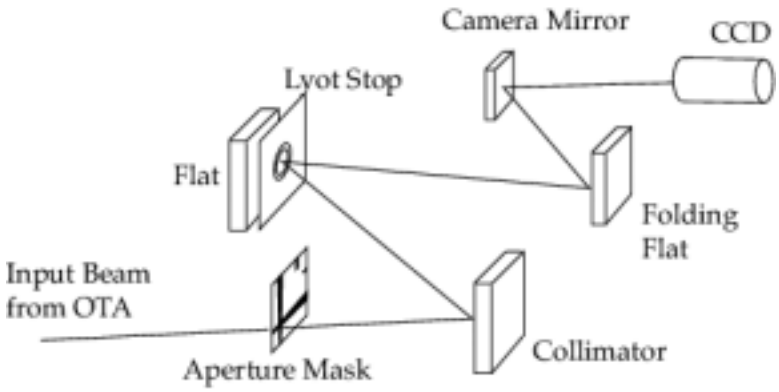

Figure 1. Simplified depiction of the optical path for STIS coronagraphic imagery, after Heap (2000).

nebulae including Herbig-Haro objects, and candidate stellar companions associated with stars spanning $0.34 \leq V \leq 15$ (Heap et al. 2000; Grady et al. 1999, 2000, 2001a,b, 2002; Schneider 2001; Mouillet et al. 2001; Danks et al. 2001). In this paper we summarize the operation, calibration, and performance of the STIS coronagraph.

2. Coronagraphic Observations

Coronagraphic observations with STIS are carried out with the star placed under one of two orthogonal wedges, or under a $3.0'' \times 10''$ bar. While the wedges vary smoothly in diameter from 0.5"-3.0" over their 50" length, a limited set of coronagraphic "apertures" has been defined to simplify planning for coronagraphic observations. These apertures are at locations where the wedges are 1.0, 1.8, 2.0, 2.5, and $2.8''$ wide (fig 2). The vertical wedge (wedge A) is oriented along the STIS CCD axis 2, the same direction as the long slits for spectroscopic observations, and parallel to the CCD charge transfer direction. This ensures that charge saturation from the stellar point spread function (PSF) at the edge of the wedge does not contaminate the bulk of the coronagraphic image. The majority of STIS coronagraphic observations have been made with this wedge.

3. Coronagraphic Data Reduction

Coronagraphic observations made with STIS typically consist of a suite of short exposures which are grouped using the CR-SPLIT optional parameter in order to avoid saturation in the vicinity of the coronagraphic wedge. This grouping facilitates cosmic-ray rejection by median filtering the images in each observation data-cube prior to coaddition. The standard CCD image reduction then follows with overscan bias subtraction, conversion to count rates, flat-fielding, dark image subtraction, bad pixel flagging and hot pixel repair. This reduction is carried out both for science target and calibration star observations, with data obtained at different spacecraft orientations reduced separately. To ensure the largest achievable dynamic range in coronagraphic data, the observations are typically obtained with GAIN = 4, which introduces a low-level video noise with a characteristic scale of 10–30 pixels (0.5–1.5″) and amplitude 0.5–1 DN. The pattern is more conspicuous in observations made since mid-2001, using the STIS side 2 electronics (Brown 2001). At this point in time, no attempt has been made to Fourier filter the coronagraphic observations, since the available algorithms are designed for full CCD observations and can introduce ringing into the images if there are high contrast, sharp structures (e.g., the wedges) in the images.

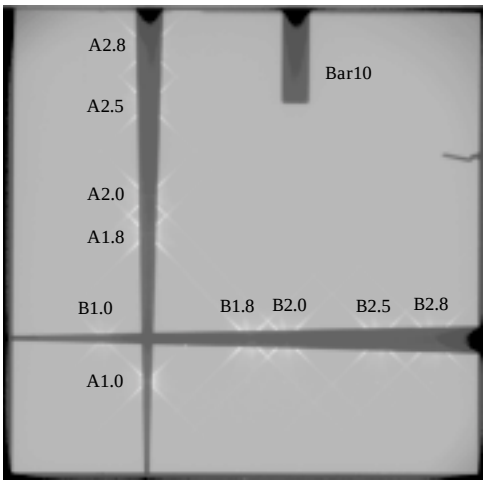

Figure 2. The STIS coronagraphic wedge structure with the "aperture" locations defined by the STScI indicated with the stellar diffraction spikes.

4. Comparison of Coronagraphic and Direct Imaging Data

The goal of coronagraphic observations is to detect faint emission near a bright star. STIS direct light images taken under these conditions are saturated near the location of the star, and along the charge transfer direction, and suffer from the presence of multiple, bright, window ghosts (Fig. 3). Use of the coronagraphic wedge enables longer exposures without saturation, and prevents formation of conspicuous window ghosts. As noted by Heap et al. (2000), the STIS Lyot stop is a circular aperture passing the central 77% of the beam area, without apodization of the diffraction spikes. All STIS images are taken with the Lyot stop in the optical path, and have PSF wings which are reduced by a factor of ≈ 2 compared to models for the optical telescope assembly. Occulting the star with the coronagraphic wedge reduces the brightness of the PSF by an additional factor of 3–5 near the star and up to an order of magnitude at distances $r \geq 10''$, but only slightly depresses the diffraction spikes, principally by reducing scattering of longer wavelength photons within the STIS CCD.

The change in the prominence of the diffraction spikes relative to the azimuthally symmetric part of the PSF is not the only change between direct-light and coronagraphic imagery with STIS. Other bright features in the STIS PSF such as the "stool legs" flanking wedge A and the "tuft" seen above wedge B in coronagraphic data obtained with that occulting bar (see Heap et al. 2000), are present in both data, but are more conspicuous in coronagraphic data. The coronagraphic PSF is sufficiently different from the direct-light PSF that direct light data *cannot be used in the reduction of STIS coronagraphic data*. Fig. 5 shows the contrast as a function of distance from the star for direct light and coronagraphic observations. Far from the star, the suppression of the PSF is similar for observations where the star is placed under the coronagraphic wedge, or off the active detector area (Fig. 6).

5. Color Dependence

The bandpass of the STIS coronagraph is the bandwidth of the unfiltered CCD, and spans 0.2–1.0 μm. The *HST* PSF is known to vary across this bandwidth, and thus it is no surprise that STIS has prominent color effects in the coronagraphic PSF. In Fig. 4 we show the PSF wings for a suite of $4.74 \leq V \leq 7.92$ single stars spanning $0.06 \leq (B-V) \leq 1.65$. The width of the observed PSF increases with increasing $(B-V)$, and is accompanied by a progressive deepening of a dark ring at $1.5''$. Subtracting a scaled PSF which differs from a

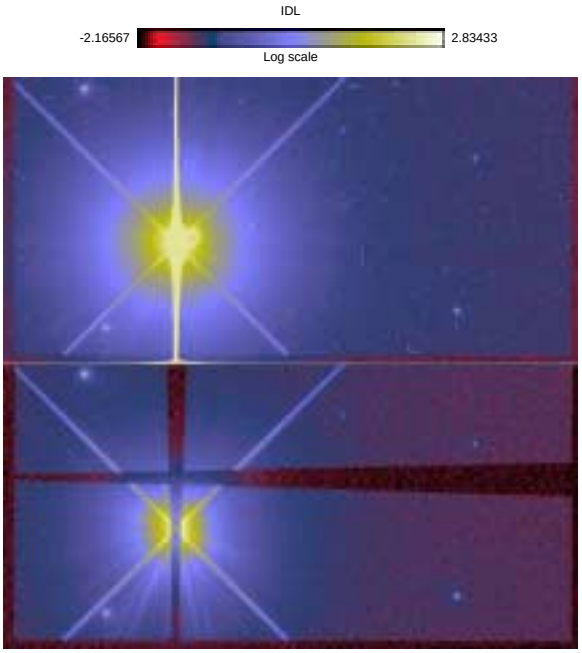

Figure 3. Comparison of direct light and coronagraphic imagery of the $V = 8.2$ Herbig Ae star HD 95881. upper) The direct light image is dominated by saturation and bleeding, and window ghosts. lower) the coronagraphic image has reduced PSF wings compared to the diffraction spikes and the high power "stool legs" flanking wedge A.

science target by $\Delta(B-V) \geq 0.08$ results in the appearance of a series of rings, resembling the diffraction rings seen in narrower-band WFPC2 or ACS imagery. Whether the ring pattern is seen as a positive or negative pattern depends upon whether the science target is bluer or redder than the PSF star. The pattern is similar along the diffraction spikes, and can be used to select comparison stars for a science target whose color is not known *a priori*.

6. Shape Dependence Upon Aperture Location

While the higher power features in STIS coronagraphic images do show some field dependence, the shape of the wings of the PSF is less dependent upon the aperture used for the observations. Comparison of PSF star observations at different wedge locations (Fig. 5) indicates that the suppression of the wings of the PSF induced by occulting the star does not depend strongly upon the wedge location, with wider wedges suppressing the inner portions of the PSF, and leaving the outer PSF wings largely unaffected. The primary advantage of using the coronagraphic wedge is to reduce the dynamic range of the image, or equivalently to go deeper by exposing longer before the CCD saturates. At wedge A1.0, exposures can extend a factor of ≈ 400 longer than for direct light images before reaching the CCD full-well. The ability to integrate longer without saturation means that fewer detector readouts are needed to build up the desired signal to noise far from the star, and hence that the read noise + sky background in the final image is lower.

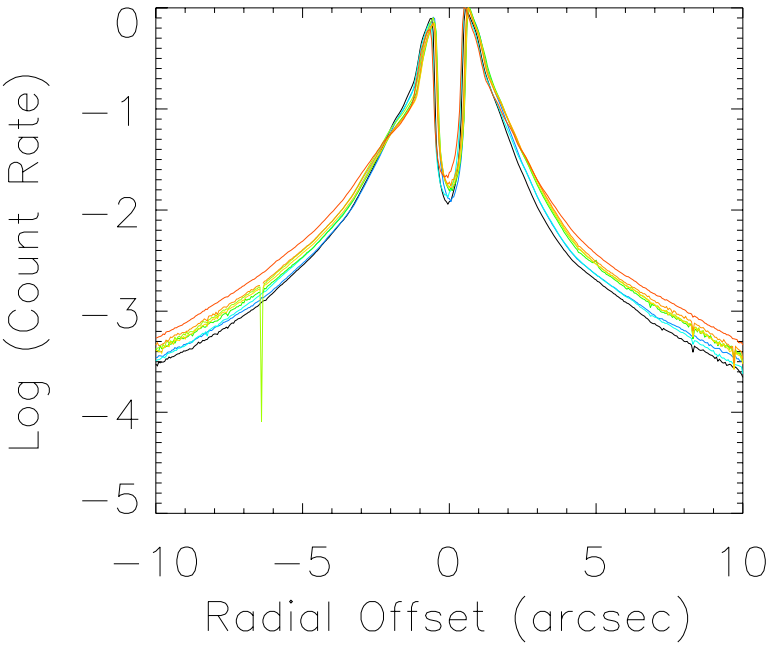

Figure 4. Dependence of the shape of the PSF wings on the stellar $(B-V)$ from $(B-V) = 0.06$ (black) through $(B-V) = 1.65$ (red).

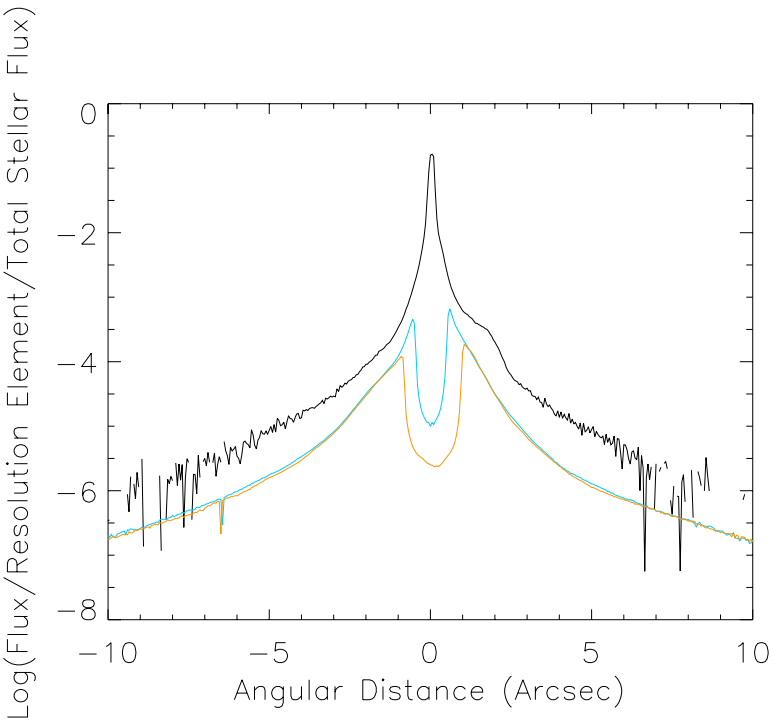

Figure 5. Comparison of the PSF radial profile for HR 4413 ($V = 5.2$) for direct light images (black), at wedge A1.0 (blue), and at wedge A1.8 (orange).

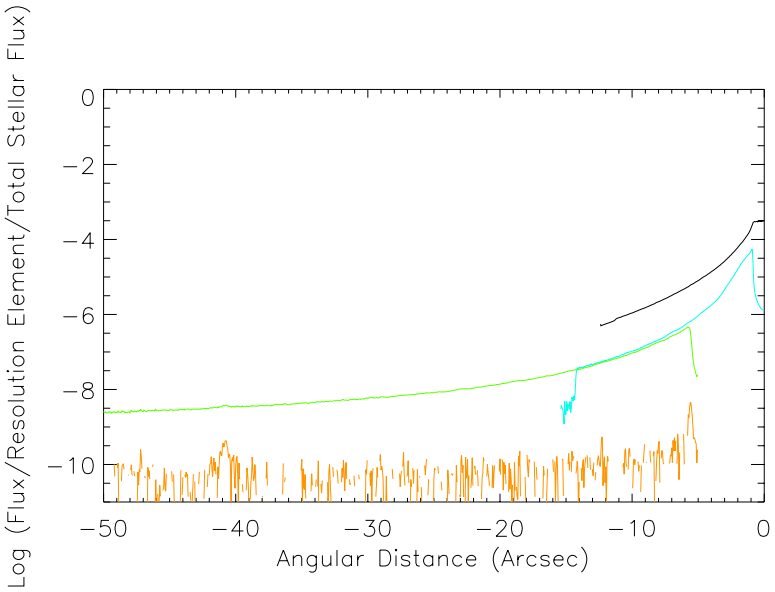

Figure 6. Suppression of the PSF wings is similar for coronagraphic images and observations where the star is placed off the active detector area. Here data are shown for ϵ Eri in direct imaging mode (black), at wedge A2.0 (blue), 5″ off the detector (green), and the contrast achieved following PSF subtraction for the off-the-detector observations.

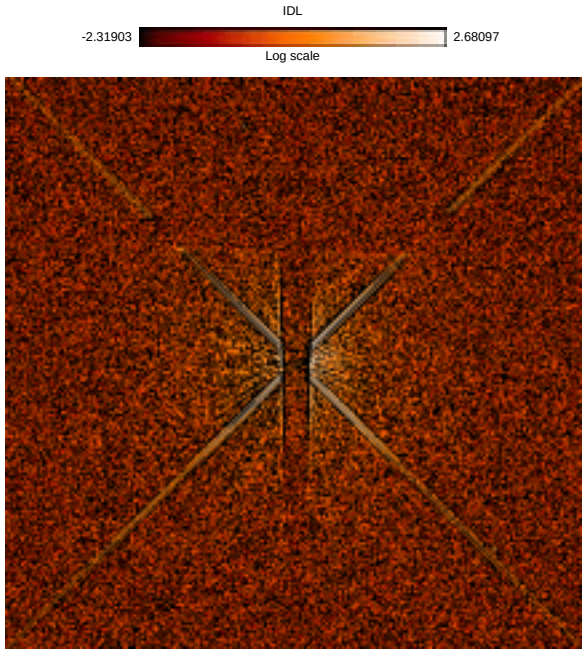

Figure 7. PSF subtraction residuals for 2 successive observations of the $V = 5.2$ star HR 4413. The image shown here is 10″ on a side. Within 2″ of the star, the radial "tendrils" dominate.

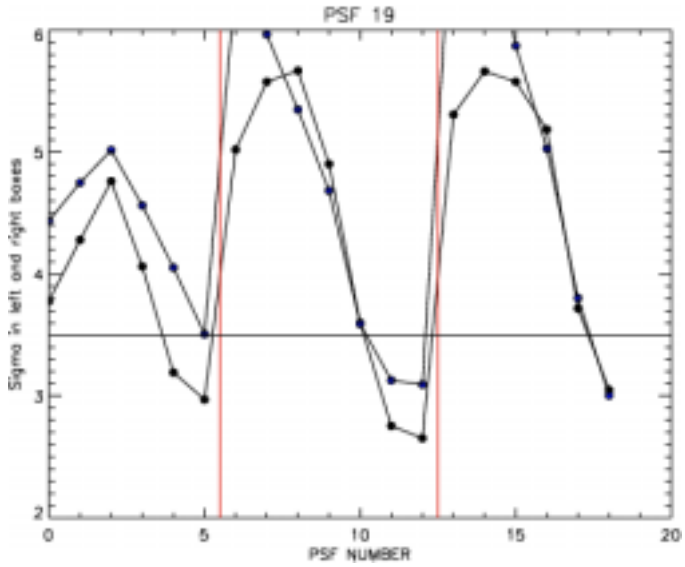

Figure 8. Variation in PSF subtraction residuals during a single 3-orbit visit to $V = 5.2$ HD 141653 relative to one of the observations from the 3rd orbit. Residuals were computed in 1 arcsec^2 boxes to the left and right of wedge A. Orbit breaks are indicated in red. STIS shows a clear orbital phase dependence which is quite different from the response of NICMOS.

7. Stability

In addition to color matching of the PSF star to the science object, successful removal of the PSF from coronagraphic observations hinges upon the extent to which the science object and the PSF star were placed at the same position behind the coronagraphic wedge, and the extent to which the *HST* and STIS are in the same alignment and focus condition in both observations. Compared to ground-based observations, the *HST* point spread function is remarkably stable, with the principal changes involving redistribution of light due to thermally-driven changes in the primary-secondary mirror separation (see discussion in Pavlovsky et al. 2001). When there is no color difference or difference in stellar placement under the wedge, net images (star-PSF star) are dominated by 1–2″ long radial features due to differences in the dispersed speckles, which Schneider has termed "tendrils" (Fig. 7). These features provide a structured, high contrast zone within 2″ of the star, and are minimized for short (e.g., bright occulted source) observations taken within a few minutes of each other, but show systematic increases in amplitude with orbital phase (Fig. 8).

8. Limiting Performance

For exo-planet searches and detection of faint nebulosity, one parameter of interest is the contrast achieved after removal of the PSF via subtraction of a comparison star. In the absence of color differences between the science target and the calibration star, at 2″ from the star we have achieved contrasts of 10^{-6} arcsec^{-2} relative to the total stellar flux. The equivalent contrast for a point source, measured over the $0.1'' \times 0.1''$ *HST* resolution element is 10^{-8}. This is achieved for back-to-back observations of the same $V = 5.2$ calibration star, with no change in telescope pointing between observations, other than the FGS jitter. The same measurement for data obtained on successive orbits with independent target acquisitions for each orbit (separate visits) is approximately a factor of 2 worse, reflecting changes in the placement of the star under the wedge. This performance is comparable

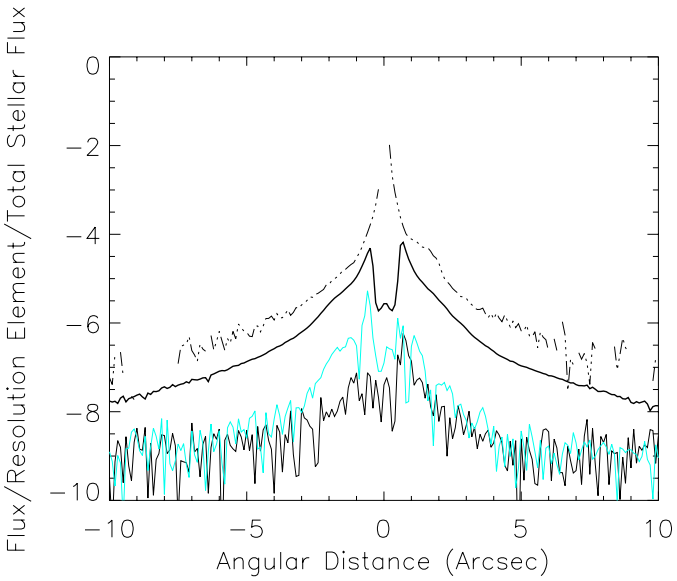

Figure 9. Star-to-Nebulosity contrast for the STIS coronagraph at $V = 5.2$. The narrow dot-dash line is the direct imaging radial profile, the narrow solid line is the raw coronagraphic radial profile. The profile following PSF subtraction for optimally positioned stars with no color mismatch and contemporaneous data is shown in bold. The limiting contrast when the observations are made as separate visits separated by months is shown in aqua. Contemporary, separate visits have radial profiles which are intermediate.

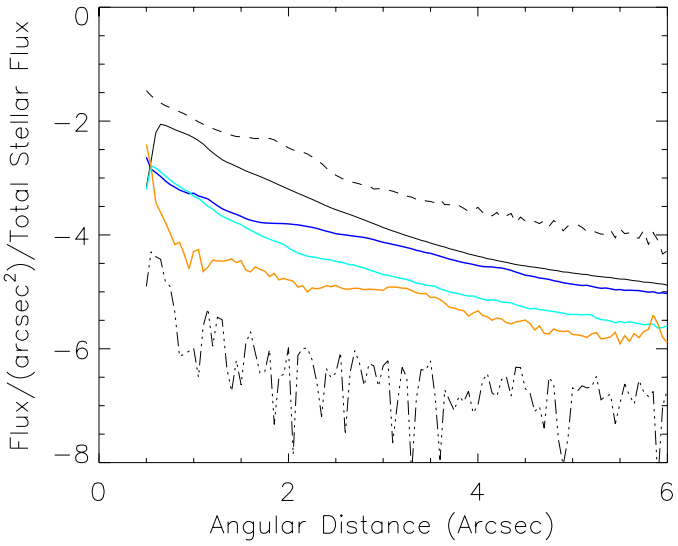

Figure 10. Radial surface brightness profiles for the Herbig Ae stars coronagraphically imaged by STIS. Dashed = direct imaging profile, black = raw coronagraphic profile, blue = AB Aur (nebulosity at $r \geq 3''$ visible in WFPC/2 direct imagery), aqua = HD 100546, orange = HD 163296. The debris disks β Pictoris and HR 4796A are close to the raw coronagraphic data profile in surface brightness, while HD 141569 A is intermediate between AB Aur and HD 163296. The dot-dashed profile is the limiting radial profile for the $V = 7$–8 Herbig Ae star non-detections. The fainter T Tauri disks that have been similarly observed have radial surface brightness closer to 10^{-3} arcsec^{-2} relative to their stars.

to that seen when the spacecraft is rolled in the middle of an orbit (Fig. 9). This latter finding differs significantly from the NICMOS experience, and reflects the fact that STIS is located on the sunny side of the HST spacecraft, in a less thermally benign environment than NICMOS or ACS.

In all cases *far from the star* the contrast relative to the star is limited by the combined effects of the sky background, detector dark counts, and more importantly, the aggregate effects of the detector read noise. Further exploration of the suitability of Fourier filtering techniques developed for studies of galaxies is needed.

9. Application to PMS Stars

To date, the principal application of the STIS coronagraphic capability has been to detect nebulosity associated with nearby, young stars. Objects that have been successfully coronagraphically imaged by STIS span $15 \leq V \leq 0.34$, and have circumstellar nebulosity, L_{CS}, which has $L_{CS}/L* = 10^{-3}$ to 10^{-5} arcsec^{-2} $2''$ from the star (Fig. 10). These include stars with nebulosity detectable in direct imaging with WFPC2 (e.g., TW Hya, Krist et al. 2000; AB Aur, Grady et al. 1999), as well as nebulosity detectable in the coronagraphic data only following PSF subtraction. This latter case includes some intrinsically faint disks (e.g., HD 163296 Grady et al. 2000) as well as objects with disks with steep radial surface brightness profiles, e.g., following r^{-3}. Comparatively small ($r \leq 2''$) disks, even when bright, present a more challenging case in that their angular extent is small compared to the STIS wedge, located in a region subject to the breathing "tendrils."

10. The STIS Coronagraph in an Era of Multiple HST Coronagraphs

HST now has 3 working coronagraphs. Compared to NICMOS, STIS offers a larger field of view, which can be important in determining where the nebulosity ends (e.g., the HD 100546 envelope, Grady et al. 2001), higher spatial resolution due to imaging at shorter wavelengths, and comparable sensitivity limits. For detection of comparatively bright, point-source companions to occulted stars, NICMOS's ability to roll in mid-orbit offers a more time-efficient observing strategy. NICMOS coronagraphic imagery can be combined with filters to provide some albedo and chemistry information.

Both ACS and STIS are optical coronagraphs. ACS offers better sampling of the image, with pixels that are a factor of 4 smaller in area than the STIS CCD pixels, and the use of filters. The sensitivity of ACS is within a factor of 2 of STIS's performance for extended objects (Pavlovsky et al. 2002). ACS will be the preferred coronagraph for large-scale ($r \geq 1''$) and brighter nebulosity where the more limited throughput in each filter is compensated for by the ability to carry out albedo studies. The limiting contrast for faint nebulosity will depend, for ACS observations, upon the impact of the re-imaged direct light on the data, and has yet to be determined. For smaller disks, such as even the larger ones around classical T Tauri stars, the large ACS spot size will occult much of the disk and also has the potential to impair recognition of the presence of an optically visible disk. Given the small advantage ACS has in apodization, STIS may still be the preferred instrument for initial surveys for disks and more extended nebulosity as a result of both the broad bandpass and equal sensitivity to reflection nebulosity and emission-line nebulae in one observation. STIS provides access to narrower occulter locations than ACS and may be the preferred instrument for optical imaging of smaller circumstellar disks.

11. Recommendations for STIS Coronagraphic Observations

- The location on wedge A used for observations of HR 4796A and HD 141569A, where the wedge has a diameter of 0.6″, should be defined as a formal aperture, to facilitate observation planning, and to minimize confusion in the archive with data taken at wedge A1.0 (the current location such observations are filed under). To optimize observations at this location, given the breathing "tendrils," observers will need to have dedicated PSF observations, so there will be no cost to the STScI, other than maintaining the aperture location calibration.

- For optimal reduction of STIS coronagraphic data, where PSF star observations are used, the PSF data should be as close a color match to the program star as feasible (and certainly with $\Delta(B-V) \leq 0.08$), and obtained on adjacent orbits.

- For STIS coronagraphic observations where the PSF of the star itself will be used in the data reduction, experience with ϵ Eri suggests that multiple spacecraft orientations, with $n \geq 4$, and preferably closer to 9–11 are needed to ensure a median PSF image which is free of contamination by background galaxies. Fewer observations are needed in the presence of bright nebulosity (see Heap et al. 2000 for β Pic).

- The practice for coronagraphic observations of bright objects has been to read out only part of the detector, to minimize detector read overheads during the orbit. Longer observations, such as are appropriate for $10 \leq V \leq 15$ T Tauri stars do not benefit appreciably from this strategy. For such observations, we recommend reading the full detector, both to give a better view of the environment of the star, and to permit use of filtering techniques to reduce the read noise.

Acknowledgments. This study has made use of calibration observations obtained as part of proposals 7088, 8037 8491, 8896, GO-9241, 8925, 8419, GO-8842, GO-9037, and GO-9136 and parallel observations of HD 95881 obtained on GO-8796. Support for the analysis under proposal HST-AR-9224 was provided by NASA through a grant from the Space Space Telescope Science Institute, which is operated by the Association of Universities for Research in Astronomy, Inc., under NASA contract NAS 5-26555. Support for the STIS IDT was provided by NASA Guaranteed Time Observer (GTO) funding to the STIS Science Team in response to NASA A/O OSSA -4-84 through the Hubble Space Telescope Project at Goddard Space Flight Center. CAG was supported through transfer of funds to The National Optical Astronomy Observatories. NOAO is operated by the Association of Universities for Research in Astronomy (AURA), Inc., under cooperative agreement with the National Science Foundation. Data analysis facilities were provided by the Laboratory for Astronomy & Solar Physics, at NASA's GSFC.

References

Brown, T. M. 2001, "STIS CCD Read Noise During Side-2 Operations," *Instrument Science Report* STIS 2001-005 (Baltimore: STScI)

Grady, C. A., Woodgate, B., Bruhweiler, F. C., Boggess, A., Plait, P., Lindler, D. J., Clampin, M., & Kalas, P. 1999, ApJ 523, L151.

Grady, C. A., Devine, D., Woodgate, B., Kimble, R., Bruhweiler, F. C., Boggess, A., Linsky, J. L., Plait, P., Clampin, M., & Kalas, P. 2000, ApJ 544, 895.

Grady, C. A., et al. 2001, AJ 122, 3396.

Heap, S. R., Lindler, D. J., Lanz, T. M., Cornett, R. H., Hubeny, I., Maran, S. P., & Woodgate, B. 2000, ApJ 539, 435.

Kimble, R. A., et al. 1998, ApJ 492, L83

Krist, J. E., Stapelfeldt, K. R., Ménard, F., Padgett, D. L., & Burrows, C. J. 2000, ApJ 538, 793.

Kuhn, J. R., Potter, D., & Parise, B. 2001, ApJ 553, L189.

Leitherer, C., et al. 2001, *STIS Instrument Handbook*, V. 5.1 at http://www.stsci.edu/instruments/stis

Lyot, M. B. 1939, MNRAS 99, 580.

Malbet, F., Yu, J. W., & Shao, M. 1995, PASP, 107, 386.

Mouillet, D., Lagrange, A. M., Augereau, J. C., & Ménard, F. 2001, A&A 372, L61.

Pavlovsky, C., et al. 2001, *ACS Instrument Handbook*, V. 2.1 at http://www.stsci.edu/instruments/acs

Schneider, G. 2001, AAS 198, 8301.

Schultz, A. B., Hart, H. M., Kochte, M., Bruhweiler, F., DiSanti, M. A., Miskey, C., Cheng, K.-P., Reinhard, K., & Schneider, G. 2001, AAS 198, 7707

Stapelfeldt, K. R., et al. 1999, ApJ 516, L95.

Woodgate, B. E., et al. 1998, PASP 110, 1183